Report

Neuron

Dendritic Spines Prevent Synaptic Voltage Clamp

Highlights

- High spine neck resistance prevents voltage-clamp control of excitatory synapses.
- Voltage-clamp measurements are severely distorted for spiny neurons.
- Large single-spine AMPA conductance saturates synaptic current.

Authors

Lou Beaulieu-Laroche, Mark T. Harnett

Correspondence

harnett@mit.edu

In Brief

Beaulieu-Laroche and Harnett demonstrate that voltage clamp, the main approach to investigate synaptic physiology, is ineffective for most synapses because they reside on electrically isolated spines.

Beaulieu-Laroche & Harnett, 2018, Neuron 97, 75–82
January 3, 2018
https://doi.org/10.1016/j.neuron.2017.11.016

CellPress

Neuron
Report

Dendritic Spines Prevent Synaptic Voltage Clamp

Lou Beaulieu-Laroche[1] and Mark T. Harnett[1,2,*]
[1]Department of Brain and Cognitive Sciences, McGovern Institute for Brain Research, Massachusetts Institute of Technology, Cambridge, MA 02139, USA
[2]Lead Contact
*Correspondence: harnett@mit.edu
https://doi.org/10.1016/j.neuron.2017.11.016

SUMMARY

Synapses are the fundamental units of information processing in the mammalian brain. Much of our understanding of their functional properties comes from voltage-clamp analysis, the predominant approach for investigating synaptic physiology. Here, we reveal that voltage clamp is completely ineffective for most excitatory synapses due to spine electrical compartmentalization. Under local dendritic voltage clamp, single-spine activation produced large spine head depolarizations that severely distorted measurements and recruited voltage-dependent channels. To overcome these voltage-clamp errors, we developed an approach to provide new, accurate measurements of synaptic conductance. Single-synapse AMPA conductance was much larger than previously appreciated, producing saturation effects on synaptic currents. We conclude that electrical compartmentalization profoundly shapes both synaptic function and how that function can be assessed with electrophysiological methods.

INTRODUCTION

Electrophysiological approaches have been instrumental in deciphering how neurons communicate through electrical signals generated at synapses. For over thirty years, voltage clamp has been the main approach to study synaptic physiology. This technique has been used to deconstruct the molecular basis of synaptic transmission and plasticity *in vitro* (Bekkers et al., 1990; Bekkers and Stevens, 1990; Benke et al., 1998; Blanton et al., 1989; Brown and Johnston, 1983; Edwards et al., 1990; Granger et al., 2013; Guzman et al., 2016; Isaac et al., 1995; Jonas et al., 1993; Malinow and Tsien, 1990; Matsuzaki et al., 2001) as well as to probe input tuning and integration *in vivo* (Adesnik, 2017; Adesnik and Scanziani, 2010; Borg-Graham et al., 1998; Chadderton et al., 2014; Froemke et al., 2007; Gan et al., 2017; Haider et al., 2006; Haider et al., 2013; Liu et al., 2011; Petersen, 2017; Sato et al., 2016; Tan and Wehr, 2009; Wehr and Zador, 2003; Wilent and Contreras, 2005; Wu et al., 2008). Voltage-clamp circuits rapidly pass current to maintain the voltage at the tip of the electrode at set values, enabling measurement of current flow through ion channels and estimation of conductance (Cole, 1949; Hamill et al., 1981). One crucial assumption for voltage-clamp analysis is that synapses are isopotential with the recording site (Johnston and Brown, 1983; Spruston et al., 1993; Williams and Mitchell, 2008). However, accumulating evidence indicates that dendritic spines, where the vast majority of excitatory synapses reside (Bourne and Harris, 2008; Ramón y Cajal, 1888), can compartmentalize electrical signals via high spine neck resistances (R_{neck}) (Acker et al., 2016; Araya et al., 2006; Bloodgood et al., 2009; Bloodgood and Sabatini, 2005; Grunditz et al., 2008; Harnett et al., 2012; Jayant et al., 2017; Palmer and Stuart, 2009; Yuste, 2013). We reasoned that electrical isolation would prevent voltage control of spiny synapses, thereby distorting measurements and calling into question our current understanding of synaptic function. Here, we demonstrate that spines cannot be voltage clamped, and subsequently develop a new approach to circumvent the problem and accurately measure synaptic conductance at single spines.

RESULTS

High Spine Neck Resistance Prevents Synaptic Voltage Control

We first determined the impact of R_{neck} on the effectiveness of synaptic voltage clamp with a simple compartmental model based on cortical layer 5 pyramidal neurons (Figure 1A; STAR Methods). For an R_{neck} of 500 MΩ based on prior estimates (Harnett et al., 2012; Jayant et al., 2017), a synaptic input resulted in a large spine EPSP (excitatory postsynaptic potential) and a much smaller dendritic EPSP under current clamp (Figure 1B). Under voltage clamp, the synaptic voltage was totally unclamped, demonstrating that high R_{neck} prevents voltage control during synaptic events. Dendritic voltage clamp recovered the current but drastically underestimated synaptic conductance because the spine voltage was not controlled (Figure 1C). Synaptic conductance (g_{syn}), which reflects the density and properties of glutamate receptors, is a key parameter governing synaptic efficacy (Araya, 2014; Koch and Poggio, 1983; Koch and Zador, 1993; Wilson, 1984). We computationally explored how different values of R_{neck} and g_{syn} would affect these results (Figures 1D–1F and S1). For a wide range of parameters, synaptic voltage escape was near complete, and the magnitude of the spine depolarization determined the fraction of synaptic conductance recovered. Together with high R_{neck}, large g_{syn} dramatically reduced the synaptic driving force as the spine

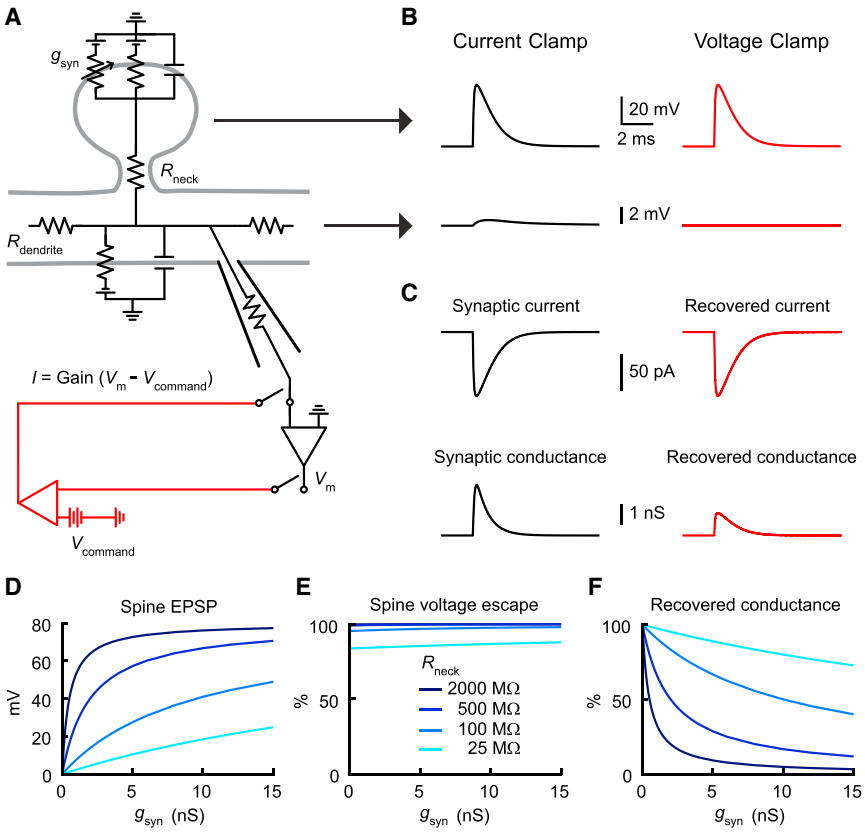

Figure 1. Impact of Spine Neck Resistance on Synaptic Voltage Clamp

(A) Equivalent circuit diagram for a spine on a dendrite. A dendritic recording at the base of the spine can switch between current clamp (black) and voltage clamp (red).

(B) Voltage in the spine (top) and dendrite (bottom) in response to a synaptic conductance change.

(C) Voltage clamp recovers the current (top) but underestimates the conductance (bottom) because the synaptic voltage is not controlled.

(D) Spine EPSP under current clamp as a function of g_{syn} for a range of R_{neck} values.

(E) Spine voltage escape under voltage clamp computed as the percentage of current-clamp spine EPSP.

(F) Recovered conductance under voltage clamp. See also Figure S1 for additional modeling results.

voltage approached reversal potential. As a result, the current entering the spine and flowing into the dendrite was saturated (Figure S1). Thus, our model predicts that voltage-clamp errors are substantial and non-uniform across synapses with varying strength and compartmentalization.

Unclamped Recruitment of Spine Voltage-Dependent Channels

To provide an experimental test of the efficacy of synaptic voltage clamp, we sought to uncover evidence of voltage escape. We hypothesized that if large unclamped spine depolarizations occur, Ca^{2+} imaging would reveal the activation of voltage-dependent channels, including NMDA receptors and voltage-gated Ca^{2+} channels (VGCCs), known to be present in spine heads (Bloodgood et al., 2009; Grunditz et al., 2008; Harnett et al., 2012; Kovalchuk et al., 2000; Sabatini et al., 2002; Yuste and Denk, 1995). To specifically assess the impact of spine compartmentalization independently of series resistance and space-clamp limitations (Armstrong and Gilly, 1992; Spruston et al., 1993; Williams and Mitchell, 2008), we performed low series resistance (11.9 ± 0.5 MΩ, n = 70) whole-cell recordings from layer 5 pyramidal neuron apical dendrites. We first tested the effectiveness of dendritic voltage clamp using an independent current-clamp electrode positioned nearby (9.8 ± 1.0 μm, n = 9) on the same dendrite (Figure 2A). With rigorous series resistance compensation (Figure S2), the voltage-clamp electrode accurately recovered injected currents and prevented voltage escape (Figures 2B and 2C). We then tested whether spines <10 μm from the electrode could be voltage clamped. Single spines were stimulated with two-photon glutamate uncaging while monitoring spine head Ca^{2+} signals with two-photon linescan imaging of Fluo-4 (Figure 2D). Under the same uncaging conditions, we observed Ca^{2+} signals of similar amplitudes under current clamp and voltage clamp, indicating that dendritic voltage clamp could not prevent spine Ca^{2+} influx (Figures 2E and 2F).

To establish that these Ca^{2+} signals were evidence of spine depolarization, we investigated the nature and voltage-dependence of the ion channels recruited. Blocking NMDA receptors (100 μM D-APV + 50 μM MK-801) drastically reduced spine head Ca^{2+} signals (Figures 2G and 2H; 28.7% ± 0.1% of baseline, n = 6), revealing that NMDA receptors are recruited during single-spine uncaging events. With AMPA receptors blocked (20 μM DNQX), strong membrane depolarization was needed to observe NMDA-mediated Ca^{2+} signals (Figure S3). Thus, NMDA receptor activation is evidence of unclamped AMPA-mediated spine depolarization. Under constant blockade of NMDA receptors, smaller Ca^{2+} signals could still be elicited with glutamate uncaging (Figure 2I). Depleting intracellular stores of Ca^{2+} (30 μM CPA + 200 μM GPN) (Padamsey et al., 2017; Sabatini et al., 2002) did not affect the transients (Figure S3). In contrast, the application of VGCC blockers (300 μM Ni^{2+} + 20 μM nimodipine) demonstrated that these Ca^{2+} signals were voltage-dependent and mediated by VGCCs (Figure S3). Their recruitment during uncaging events was again similar under current clamp and voltage clamp (Figures 2I and 2J), providing additional evidence of synaptic voltage escape.

Spine-to-dendrite voltage attenuation is mediated by dendritic impedance (Gulledge et al., 2012; Harnett et al., 2012), and we performed these experiments on low-impedance trunk dendrites where attenuation is large. Our experimentally constrained model suggests that dendritic properties have little influence on voltage-clamp performance (Figure S4). Filling the dendrites with a cesium-based intracellular solution to increase the

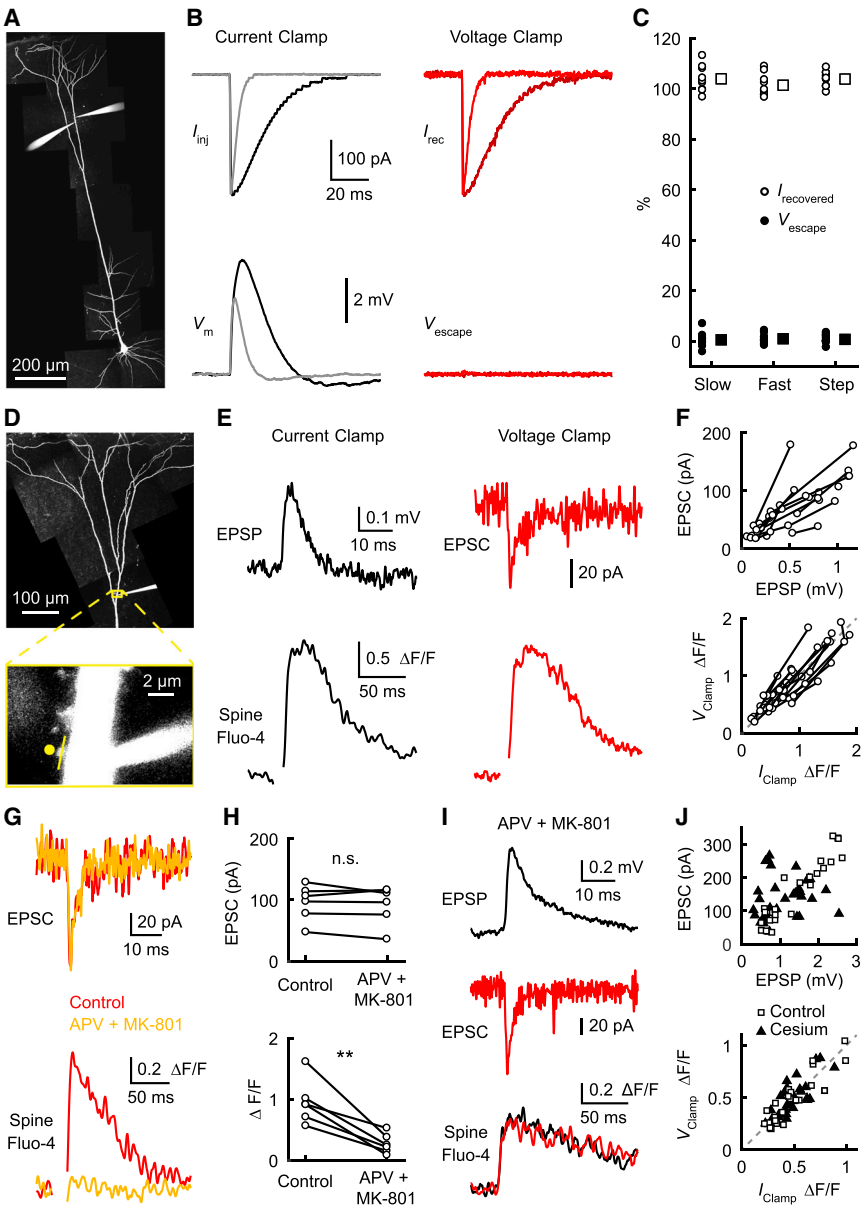

Figure 2. Unclamped Spine Depolarization Recruits Voltage-Dependent Channels

(A) Two-photon image of a dual-dendritic recording 860 µm from the soma.

(B) Under current clamp, slow and fast EPSC-shaped current injections depolarize the dendrite. Under voltage clamp, the same current injections are faithfully recovered and there is little voltage escape.

(C) Recovered current (white) and voltage escape (black) for slow and fast EPSC-shaped as well as step current injections (n = 9 dendrites). Pooled data are represented as mean ± SEM. See also Figure S2 for the impact of series resistance compensation.

(D) Image of a dendritic recording 600 µm from the soma. The yellow box shows the spine linescan imaging (yellow line) and glutamate uncaging (yellow dot). See also Figure S2 for uncaging resolution.

(E) Uncaging-evoked dendritic EPSP/EPSC and corresponding spine Ca^{2+} signal under current clamp (black) and voltage clamp (red).

(F) Top, relationship between EPSP and EPSC (n = 37, 18 spines stimulated at 1–3 laser intensities). Bottom, corresponding spine Ca^{2+} signals under current clamp and voltage clamp are not different (n = 19, p = 0.58, paired t test for highest laser intensity).

(G) Dendritic EPSCs and spine Ca^{2+} signals before (red) and after the application of D-APV and MK-801 to block NMDA receptors (orange).

(H) D-APV and MK-801 application significantly reduced the spine Ca^{2+} signals (n = 6, **p = 0.0036, paired t test). The EPSCs are not different (n = 6, p = 0.42, paired t test), likely because AMPA currents dominate the small NMDA currents (Figure S3).

(I) Uncaging-evoked dendritic EPSP/EPSC and spine Ca^{2+} signals mediated by VGCCs (D-APV and MK-801 are present to block NMDA receptors). See also Figure S3 for the contribution of VGCCs.

(J) Top, relationship between EPSP and EPSC with a control (white squares) or with a cesium-based intracellular solution (black triangles). Bottom, spine Ca^{2+} signals are not different under current clamp and voltage clamp (control: n = 18, p = 0.90, paired t test; cesium: n = 27, p = 0.19, paired t test). See also Figure S4 for simulations and experiments in higher impedance dendrites.

dendritic impedance did not improve voltage clamp (Figures 2J and S4). In addition, we performed experiments on higher impedance basal dendrites during somatic voltage-clamp recordings (Figure S4). Spine depolarization, as well as dendritic spikes, could not be prevented by voltage clamp under those conditions. Thus, spines throughout the dendritic arbor cannot be voltage clamped.

Measurement of Synaptic Conductance at Single Spines

Voltage clamp is ineffective at spines, but how does this affect measurements of synaptic conductance? The answer strongly depends on the magnitude of the unclamped spine depolarization (Figure S1). To quantitatively address this issue, we devised a method to measure spine voltage during synaptic activation (STAR Methods). Following Ohm's law, the current flowing from the spine into the dendrite is a function of R_{neck} and the voltage difference between the two electrical compartments. Under voltage clamp, the dendritic voltage is constant. Therefore, the spine EPSP and the recovered current are linearly related (Figure 3A). Interestingly, rather than directly reflecting synaptic conductance, we discovered that voltage-clamp current measurements reflect the unclamped spine EPSP (Figure 3B). We exploited this relationship to estimate AMPA-mediated spine EPSPs evoked by glutamate uncaging. First, we uncaged on a single spine to elicit VGCC-mediated spine Ca^{2+} transients under current clamp and voltage clamp (Figures 3D and 3E). Next, we injected artificial excitatory postsynaptic currents (aEPSCs) with one electrode and recorded the resulting

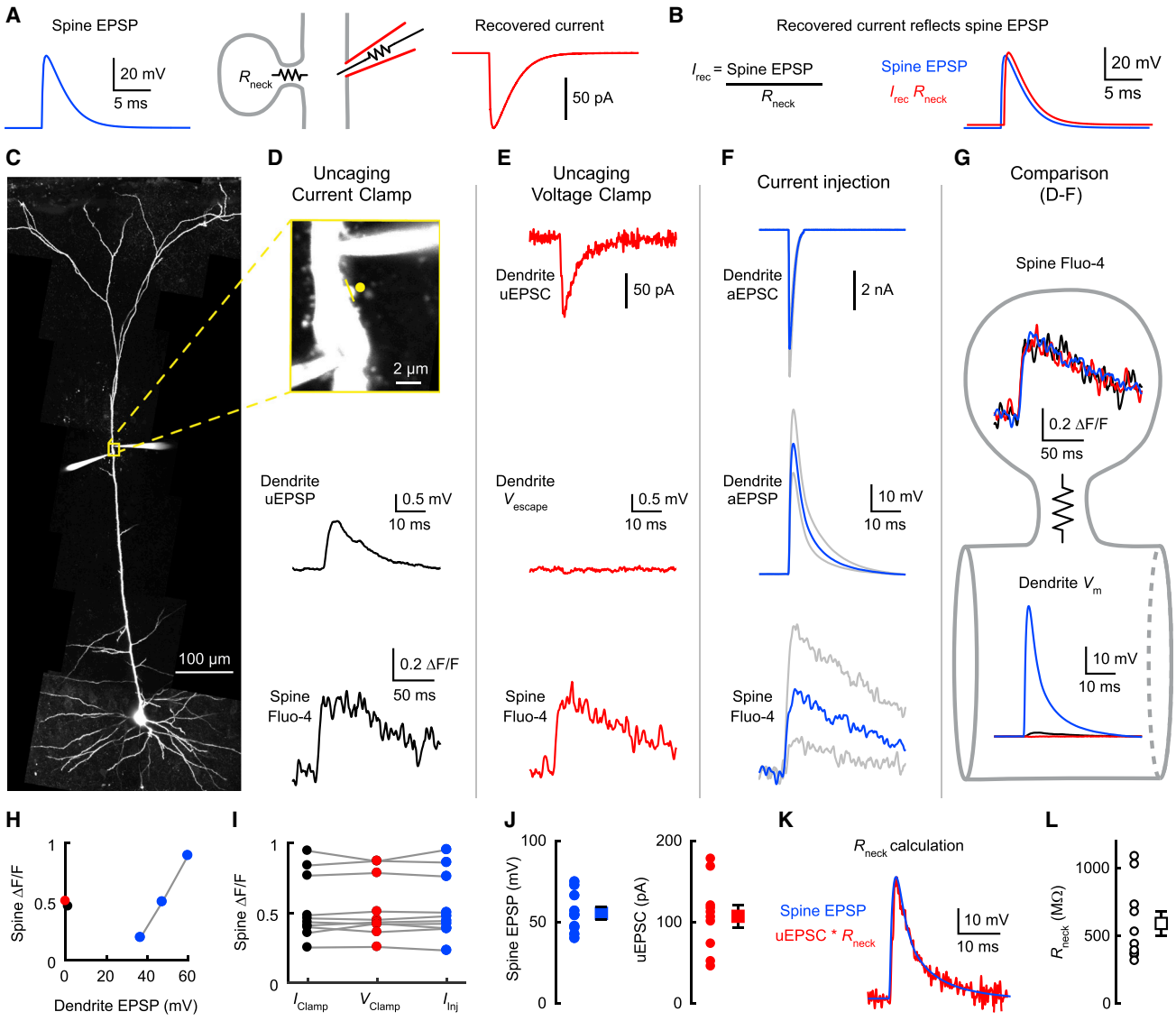

Figure 3. Measurement of Spine Voltage Escape

(A) Relationship between the spine EPSP and the recovered current under voltage clamp. See STAR Methods for details.

(B) The recovered current and the spine EPSP have identical kinetics.

(C) Image of a dual dendritic recording 490 µm from the soma.

(D) Top, yellow box from (C) expanded to show the two electrodes and the spine linescan imaging (yellow line) and glutamate uncaging (yellow dot). Uncaging-evoked dendritic EPSP (uEPSP; middle) and spine Ca^{2+} signal (bottom) in the presence of TTX, D-APV, and MK-801.

(E) Top, uncaging-evoked dendritic EPSC (uEPSC). Middle, dendritic voltage escape measured with an independent electrode. Bottom, spine Ca^{2+} signal.

(F) Artificial EPSCs (aEPSCs; top) are injected in the dendrite to produce artificial EPSPs (aEPSPs; middle) with kinetics matching the uEPSC and spine Ca^{2+} signals (bottom) matching the uncaging ones.

(G) Comparison of the spine Ca^{2+} signals and dendritic potentials from (D)–(F).

(H) Spine head Ca^{2+} signals as a function of dendritic EPSP.

(I) Spine Ca^{2+} signals across conditions (n = 10).

(J) Distribution of spine EPSP and uEPSC.

(K) Method to calculate R_{neck}.

(L) R_{neck} estimates. Pooled data are represented as mean ± SEM.

artificial EPSPs (aEPSPs) with a nearby second electrode (Figure 3F; STAR Methods). The kinetics and amplitude of the aEPSPs were calibrated to have a similar temporal profile as the uncaging EPSC (uEPSC) (Figure 3K) and to elicit spine Ca^{2+} signals matching those produced by the glutamate uncaging (Figures 3G–3I). We performed these experiments with a cesium-based intracellular solution and in the presence of TTX (0.5 µM), D-APV (50–100 µM), and MK-801 (10–25 µM) to isolate

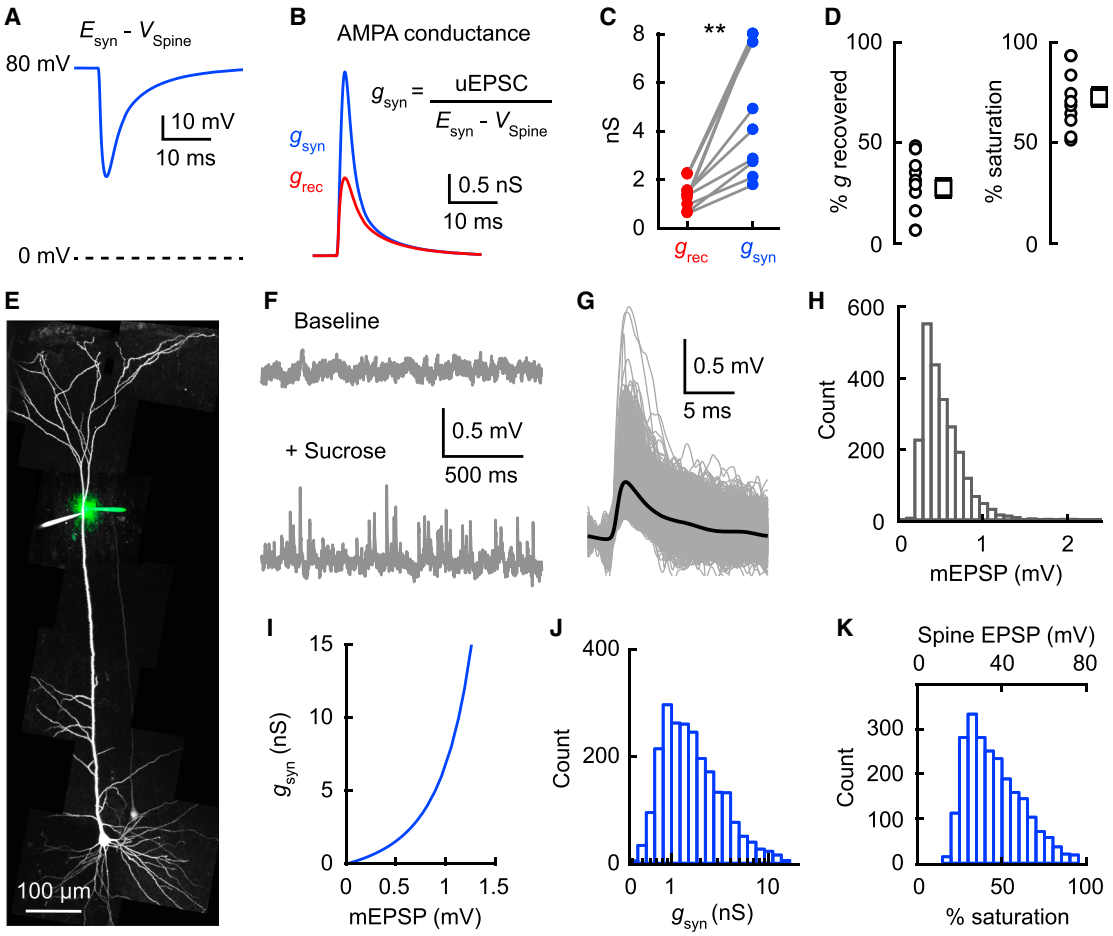

Figure 4. Single-Spine AMPA Conductance

(A) Driving force during the synaptic event from Figure 3K.

(B) Estimated AMPA conductance (blue) and distorted conductance recovered by voltage clamp (red).

(C) Left, comparison of recovered (red) and estimated AMPA conductance (blue) (n = 10, **p = 0.0020, Wilcoxon paired test).

(D) Left, percentage of conductance recovered by voltage clamp. Right, percentage of current saturation. Pooled data are represented as mean ± SEM.

(E) Dendritic recording 618 µm from the soma. A second pipette (green) filled with high-osmolality sucrose-aCSF to evoke mEPSPs is positioned extracellularly nearby.

(F) Baseline recording (top) and recording during the application of sucrose-aCSF (bottom).

(G) Recorded mEPSPs with the average in black.

(H) Distribution of mEPSP amplitudes (n = 2285 events from 4 neurons).

(I) Transfer function from mEPSP to g_{syn} for a constant R_{neck} of 590 MΩ. See also Figure S1.

(J) Inferred distribution of g_{syn} based on the distribution of mEPSPs in (H) and the transfer function in (I).

(K) Current saturation for the inferred distribution of g_{syn} in (J). The saturation of the current is directly proportional to the spine EPSP. See also Figure S5.

AMPA-mediated potentials and VGCC-mediated Ca^{2+} signals. Owing to the lack of attenuation from the dendrite to the spine (Harnett et al., 2012; Koch and Zador, 1993; Rall, 1974), the matched aEPSP provided an accurate estimate of the spine voltage during glutamate uncaging. Despite effective dendritic voltage clamp (4.6% ± 1.7% dendritic voltage escape, n = 10), we computed very large uncaging-evoked spine EPSP (Figure 3J; 55.3 ± 3.9 mV, n = 10), suggesting strong electrical isolation imposed by high R_{neck} values (Figures 3K and 3L; 588 ± 89 MΩ, n = 10).

Using our measurements of uncaging-evoked spine EPSPs, we estimated single-spine AMPA conductance. Conductance is a function of the current and the driving force, which is the difference between the synaptic voltage and the reversal potential (we measured E_{syn} to be 18.2 ± 2.0 mV under our conditions, n = 11). Because of the large unclamped spine depolarization, the driving force drops substantially during synaptic events (Figure 4A). We reasoned that g_{syn} could be reconstructed from the time-varying driving force and the recovered current (Figure 4B; STAR Methods). We found single-spine synaptic conductance to be much larger than what was recovered by voltage clamp (Figures 4B–4D), providing concrete evidence that voltage-clamp measurements are severely distorted. Strikingly, this conductance substantially saturated the synaptic currents (Figure 4D;

71.9% ± 4.7%, n = 10), reducing the dendritic and somatic impact of the synapse.

Finally, we estimated physiological AMPA conductance evoked by presynaptic vesicle release. We first recorded miniature EPSPs (mEPSPs) (Figures 4E–4H) induced by focal application of high-osmolality sucrose-aCSF (Bekkers et al., 1990; Larkum et al., 2009; Magee and Cook, 2000). Based on our measurement of R_{neck} and dendritic properties (Figure S1), we then built a transfer function to relate spine AMPA conductance to dendritic mEPSP (Figures 4I and S1). We inferred that physiological single-synapse AMPA conductance is much larger (Figure 4J; median, 1.47 nS; Q1–Q3, 0.95–2.53 nS; n = 2,285) than previously estimated (Bekkers et al., 1990; Guzman et al., 2016). Moreover, saturation was still substantial (Figure 4K; median, 42.4%; Q1–Q3, 32.2%–55.9%; n = 2,285). Together, these data directly demonstrate that spine saturation of synaptic currents distorts voltage-clamp accuracy under physiological conditions, which will affect many common synaptic analyses, including excitatory-inhibitory balance and synaptic plasticity (Figure S5).

DISCUSSION

Key to assessing synaptic properties with voltage clamp is keeping the membrane potential constant. Here we demonstrate that this is not possible for most excitatory synapses because they reside on electrically isolated spines. Unlike space-clamp limitations that are often thought to mainly affect distal inputs in large neurons, spine compartmentalization results in total voltage escape regardless of dendritic location in all neurons with compartmentalized spines, including cortical pyramidal neurons, CA1 pyramidal neurons (Harnett et al., 2012), dopaminergic neurons (Hage et al., 2016) and olfactory granule cells (Bywalez et al., 2015). Our results thus question the utility of whole-cell voltage clamp in spiny neurons. In addition to preventing accurate measurements of conductance and conductance-voltage relationships, the inability to voltage clamp spines has important implications for numerous common analyses in synaptic physiology. First, analyses requiring precise measurements, such as nonstationary fluctuation analysis (NSFA), will be heavily distorted by spine compartmentalization. NSFA analyzes the amplitude and variance of synaptic currents to estimate parameters such as the number and unitary conductance of synaptic receptors (Benke et al., 1998; Benke et al., 2001; Lüthi et al., 1999; Matsuzaki et al., 2001; Smith et al., 2003). Synaptic voltage escape will change the driving force and the amplitude of single-channel currents. As a result, the peak and slope of the current-variance curve will be profoundly altered, precluding accurate measurements. Second, assessments of excitatory (E) to inhibitory (I) ratio, which is thought to play a central role in controlling circuit dynamics (Adesnik, 2017; Adesnik and Scanziani, 2010; Borg-Graham et al., 1998; Froemke et al., 2007; Gan et al., 2017; Haider et al., 2006; Haider et al., 2013; Liu et al., 2011; Sato et al., 2016; Tan and Wehr, 2009; Wehr and Zador, 2003; Wilent and Contreras, 2005; Wu et al., 2008), will be severely compromised. Most inhibitory inputs are located directly onto dendrites and will not be affected by spine compartmentalization. Thus, recordings will be distorted for excitatory synapses but not for shaft inhibitory synapses, drastically shifting the perceived E/I ratio (Figure S5). Moreover, inhibitory synapses located directly on spines (Chen et al., 2012; Chiu et al., 2013; Villa et al., 2016) will interact with excitatory ones (Poleg-Polsky and Diamond, 2011), further distorting both E and I measurements (Figure S5). Finally, changes in R_{neck} and other spine conductances will affect voltage-clamp currents at hyperpolarized potentials (Figure S5), which are thought to reflect AMPA conductance. Consequently, postsynaptic plasticity phenomena often ascribed to changes in the number or properties of AMPA receptors (Malenka and Bear, 2004; Malinow and Malenka, 2002; Nicoll and Roche, 2013) may have alternative explanations.

By estimating R_{neck} and g_{syn} for individual dendritic spines, we provide new insights into the electrical impact of spines on synaptic transmission. Early theoretical inquiries indicated that the relative magnitude of g_{neck} ($1/R_{neck}$) and g_{syn} controls the electrical behavior of synapses (Harris and Stevens, 1989; Koch and Poggio, 1983; Koch and Zador, 1993; Miller et al., 1985; Wilson, 1984). If g_{syn} is very small relative to g_{neck}, spines behave as current sources, and the magnitude of the dendritic event is governed by g_{syn}. However, if g_{syn} is much larger, spines can be approximated as voltage sources, and g_{neck} controls the dendritic depolarization. It remains unclear until now under which regime spines operate because R_{neck} has been a matter of debate (Acker et al., 2016; Araya et al., 2006; Araya et al., 2014; Bloodgood et al., 2009; Bloodgood and Sabatini, 2005; Grunditz et al., 2008; Harnett et al., 2012; Jayant et al., 2017; Kwon et al., 2017; Palmer and Stuart, 2009; Popovic et al., 2015; Svoboda et al., 1996; Tønnesen et al., 2014; Yuste, 2013) and g_{syn} has not been well defined at single spines. Here, we demonstrate that large spine depolarizations recruit voltage-dependent channels without dendritic depolarization. This can only be explained by strong electrical isolation via high R_{neck} (~300–1000 MΩ), which is consistent with recent electrical recordings from dendritic spines (Jayant et al., 2017). Previous somatic voltage-clamp experiments have reported conductance around 0.2–0.5 nS for unitary synaptic contacts (Bekkers et al., 1990; Guzman et al., 2016). Our results indicate that single spiny synapses are much stronger (~1–2.5 nS), saturating postsynaptic events (~42%) and significantly reducing their ultimate somatic impact. Interestingly, we observed that the ratio of g_{neck} to g_{syn} is close to 1 (mean g_{neck} = 1.70 ns; median g_{syn} = 1.47 ns). With comparable magnitude, g_{neck} and g_{syn} control synaptic current and spine EPSP. Moreover, coordinated changes of both parameters can potently increase synaptic current while maintaining constant spine depolarization (Figure S5), which may be important to ensure consistent recruitment of spine voltage-dependent conductances. Thus, R_{neck} and g_{syn} are within an optimal functional range allowing both synaptic receptors and spine neck to tightly control spine and dendritic EPSPs to govern synaptic efficacy and plasticity.

In summary, we report that voltage-clamp analysis is incompatible with excitatory synapses on spines, highlighting the critical need to consider the compartmentalized nature of synaptic integration in designing and interpreting electrophysiological experiments. Our results provide important constraints for biophysically realistic modeling of neuronal circuits and have significant implications for future experimental approaches to analyze synaptic function.

STAR★METHODS

Detailed methods are provided in the online version of this paper and include the following:

- KEY RESOURCES TABLE
- CONTACT FOR REAGENT AND RESOURCE SHARING
- EXPERIMENTAL MODEL AND SUBJECT DETAILS
- METHOD DETAILS
  - Cortical Slice Preparation
  - Patch-Clamp Recording
  - Two-Photon Imaging and Uncaging
  - Pharmacology
  - Compartmental Modeling
  - Determination of R_{neck} and g_{syn}
- QUANTIFICATION AND STATISTICAL ANALYSES

SUPPLEMENTAL INFORMATION

Supplemental Information includes five figures and can be found with this article online at https://doi.org/10.1016/j.neuron.2017.11.016.

AUTHOR CONTRIBUTIONS

L.B.L. performed all experiments, analyses, and simulations. L.B.L. and M.T.H. conceived the project and wrote the paper.

ACKNOWLEDGMENTS

We thank Jakob Voigts for help with compartmental modeling, the laboratory of Mark Bear for the loan of equipment, Robert Desimone, Michale Fee, Stephen Williams, Charles Jennings, Michael Tadross and Michael Roberts for comments on the manuscript, and members of the Harnett laboratory for constructive criticism.

Received: August 4, 2017
Revised: October 4, 2017
Accepted: November 10, 2017
Published: December 14, 2017

REFERENCES

Acker, C.D., Hoyos, E., and Loew, L. (2016). EPSPs Measured in Proximal Dendritic Spines of Cortical Pyramidal Neurons. eNeuro *3*, ENEURO.0050-15.2016, https://doi.org/10.1523/ENEURO.0050-15.2016.

Adesnik, H. (2017). Synaptic Mechanisms of Feature Coding in the Visual Cortex of Awake Mice. Neuron *95*, 1147–1159.e4.

Adesnik, H., and Scanziani, M. (2010). Lateral competition for cortical space by layer-specific horizontal circuits. Nature *464*, 1155–1160.

Araya, R. (2014). Input transformation by dendritic spines of pyramidal neurons. Front. Neuroanat. *8*, 141.

Araya, R., Jiang, J., Eisenthal, K.B., and Yuste, R. (2006). The spine neck filters membrane potentials. Proc. Natl. Acad. Sci. USA *103*, 17961–17966.

Araya, R., Vogels, T.P., and Yuste, R. (2014). Activity-dependent dendritic spine neck changes are correlated with synaptic strength. Proc. Natl. Acad. Sci. USA *111*, E2895–E2904.

Armstrong, C.M., and Gilly, W.F. (1992). Access resistance and space clamp problems associated with whole-cell patch clamping. Methods Enzymol. *207*, 100–122.

Bekkers, J.M., and Stevens, C.F. (1990). Presynaptic mechanism for long-term potentiation in the hippocampus. Nature *346*, 724–729.

Bekkers, J.M., Richerson, G.B., and Stevens, C.F. (1990). Origin of variability in quantal size in cultured hippocampal neurons and hippocampal slices. Proc. Natl. Acad. Sci. USA *87*, 5359–5362.

Benke, T.A., Lüthi, A., Isaac, J.T., and Collingridge, G.L. (1998). Modulation of AMPA receptor unitary conductance by synaptic activity. Nature *393*, 793–797.

Benke, T.A., Lüthi, A., Palmer, M.J., Wikström, M.A., Anderson, W.W., Isaac, J.T., and Collingridge, G.L. (2001). Mathematical modelling of non-stationary fluctuation analysis for studying channel properties of synaptic AMPA receptors. J. Physiol. *537*, 407–420.

Blanton, M.G., Lo Turco, J.J., and Kriegstein, A.R. (1989). Whole cell recording from neurons in slices of reptilian and mammalian cerebral cortex. J. Neurosci. Methods *30*, 203–210.

Bloodgood, B.L., and Sabatini, B.L. (2005). Neuronal activity regulates diffusion across the neck of dendritic spines. Science *310*, 866–869.

Bloodgood, B.L., Giessel, A.J., and Sabatini, B.L. (2009). Biphasic synaptic Ca influx arising from compartmentalized electrical signals in dendritic spines. PLoS Biol. *7*, e1000190.

Borg-Graham, L.J., Monier, C., and Frégnac, Y. (1998). Visual input evokes transient and strong shunting inhibition in visual cortical neurons. Nature *393*, 369–373.

Bourne, J.N., and Harris, K.M. (2008). Balancing structure and function at hippocampal dendritic spines. Annu. Rev. Neurosci. *31*, 47–67.

Brown, T.H., and Johnston, D. (1983). Voltage-clamp analysis of mossy fiber synaptic input to hippocampal neurons. J. Neurophysiol. *50*, 487–507.

Bywalez, W.G., Patirniche, D., Rupprecht, V., Stemmler, M., Herz, A.V., Pálfi, D., Rózsa, B., and Egger, V. (2015). Local postsynaptic voltage-gated sodium channel activation in dendritic spines of olfactory bulb granule cells. Neuron *85*, 590–601.

Chadderton, P., Schaefer, A.T., Williams, S.R., and Margrie, T.W. (2014). Sensory-evoked synaptic integration in cerebellar and cerebral cortical neurons. Nat. Rev. Neurosci. *15*, 71–83.

Chen, J.L., Villa, K.L., Cha, J.W., So, P.T., Kubota, Y., and Nedivi, E. (2012). Clustered dynamics of inhibitory synapses and dendritic spines in the adult neocortex. Neuron *74*, 361–373.

Chiu, C.Q., Lur, G., Morse, T.M., Carnevale, N.T., Ellis-Davies, G.C., and Higley, M.J. (2013). Compartmentalization of GABAergic inhibition by dendritic spines. Science *340*, 759–762.

Cole, K.S. (1949). Dynamic electrical characteristics of the squid axon membrane. Arch. Sci. Physiol. (Paris) *3*, 253–258.

Edwards, F.A., Konnerth, A., and Sakmann, B. (1990). Quantal analysis of inhibitory synaptic transmission in the dentate gyrus of rat hippocampal slices: a patch-clamp study. J. Physiol. *430*, 213–249.

Froemke, R.C., Merzenich, M.M., and Schreiner, C.E. (2007). A synaptic memory trace for cortical receptive field plasticity. Nature *450*, 425–429.

Gan, J., Weng, S.M., Pernía-Andrade, A.J., Csicsvari, J., and Jonas, P. (2017). Phase-Locked Inhibition, but Not Excitation, Underlies Hippocampal Ripple Oscillations in Awake Mice In Vivo. Neuron *93*, 308–314.

Granger, A.J., Shi, Y., Lu, W., Cerpas, M., and Nicoll, R.A. (2013). LTP requires a reserve pool of glutamate receptors independent of subunit type. Nature *493*, 495–500.

Grunditz, A., Holbro, N., Tian, L., Zuo, Y., and Oertner, T.G. (2008). Spine neck plasticity controls postsynaptic calcium signals through electrical compartmentalization. J. Neurosci. *28*, 13457–13466.

Gulledge, A.T., Carnevale, N.T., and Stuart, G.J. (2012). Electrical advantages of dendritic spines. PLoS ONE *7*, e36007.

Guzman, S.J., Schlögl, A., Frotscher, M., and Jonas, P. (2016). Synaptic mechanisms of pattern completion in the hippocampal CA3 network. Science *353*, 1117–1123.

Hage, T.A., Sun, Y., and Khaliq, Z.M. (2016). Electrical and Ca(2+) signaling in dendritic spines of substantia nigra dopaminergic neurons. eLife *5*, e13905.

Haider, B., Duque, A., Hasenstaub, A.R., and McCormick, D.A. (2006). Neocortical network activity in vivo is generated through a dynamic balance of excitation and inhibition. J. Neurosci. *26*, 4535–4545.

Haider, B., Häusser, M., and Carandini, M. (2013). Inhibition dominates sensory responses in the awake cortex. Nature *493*, 97–100.

Hamill, O.P., Marty, A., Neher, E., Sakmann, B., and Sigworth, F.J. (1981). Improved patch-clamp techniques for high-resolution current recording from cells and cell-free membrane patches. Pflugers Arch. *391*, 85–100.

Harnett, M.T., Makara, J.K., Spruston, N., Kath, W.L., and Magee, J.C. (2012). Synaptic amplification by dendritic spines enhances input cooperativity. Nature *491*, 599–602.

Harnett, M.T., Xu, N.L., Magee, J.C., and Williams, S.R. (2013). Potassium channels control the interaction between active dendritic integration compartments in layer 5 cortical pyramidal neurons. Neuron *79*, 516–529.

Harris, K.M., and Stevens, J.K. (1989). Dendritic spines of CA 1 pyramidal cells in the rat hippocampus: serial electron microscopy with reference to their biophysical characteristics. J. Neurosci. *9*, 2982–2997.

Isaac, J.T., Nicoll, R.A., and Malenka, R.C. (1995). Evidence for silent synapses: implications for the expression of LTP. Neuron *15*, 427–434.

Jayant, K., Hirtz, J.J., Plante, I.J., Tsai, D.M., De Boer, W.D., Semonche, A., Peterka, D.S., Owen, J.S., Sahin, O., Shepard, K.L., and Yuste, R. (2017). Targeted intracellular voltage recordings from dendritic spines using quantum-dot-coated nanopipettes. Nat. Nanotechnol. *12*, 335–342.

Ji, N., Magee, J.C., and Betzig, E. (2008). High-speed, low-photodamage nonlinear imaging using passive pulse splitters. Nat. Methods *5*, 197–202.

Johnston, D., and Brown, T.H. (1983). Interpretation of voltage-clamp measurements in hippocampal neurons. J. Neurophysiol. *50*, 464–486.

Jonas, P., Major, G., and Sakmann, B. (1993). Quantal components of unitary EPSCs at the mossy fibre synapse on CA3 pyramidal cells of rat hippocampus. J. Physiol. *472*, 615–663.

Koch, C., and Poggio, T. (1983). A theoretical analysis of electrical properties of spines. Proc. R. Soc. Lond. B Biol. Sci. *218*, 455–477.

Koch, C., and Zador, A. (1993). The function of dendritic spines: devices subserving biochemical rather than electrical compartmentalization. J. Neurosci. *13*, 413–422.

Kovalchuk, Y., Eilers, J., Lisman, J., and Konnerth, A. (2000). NMDA receptor-mediated subthreshold Ca(2+) signals in spines of hippocampal neurons. J. Neurosci. *20*, 1791–1799.

Kwon, T., Sakamoto, M., Peterka, D.S., and Yuste, R. (2017). Attenuation of Synaptic Potentials in Dendritic Spines. Cell Rep. *20*, 1100–1110.

Larkum, M.E., Nevian, T., Sandler, M., Polsky, A., and Schiller, J. (2009). Synaptic integration in tuft dendrites of layer 5 pyramidal neurons: a new unifying principle. Science *325*, 756–760.

Liu, B.H., Li, Y.T., Ma, W.P., Pan, C.J., Zhang, L.I., and Tao, H.W. (2011). Broad inhibition sharpens orientation selectivity by expanding input dynamic range in mouse simple cells. Neuron *71*, 542–554.

Lüthi, A., Chittajallu, R., Duprat, F., Palmer, M.J., Benke, T.A., Kidd, F.L., Henley, J.M., Isaac, J.T., and Collingridge, G.L. (1999). Hippocampal LTD expression involves a pool of AMPARs regulated by the NSF-GluR2 interaction. Neuron *24*, 389–399.

Magee, J.C., and Cook, E.P. (2000). Somatic EPSP amplitude is independent of synapse location in hippocampal pyramidal neurons. Nat. Neurosci. *3*, 895–903.

Malenka, R.C., and Bear, M.F. (2004). LTP and LTD: an embarrassment of riches. Neuron *44*, 5–21.

Malinow, R., and Malenka, R.C. (2002). AMPA receptor trafficking and synaptic plasticity. Annu. Rev. Neurosci. *25*, 103–126.

Malinow, R., and Tsien, R.W. (1990). Presynaptic enhancement shown by whole-cell recordings of long-term potentiation in hippocampal slices. Nature *346*, 177–180.

Matsuzaki, M., Ellis-Davies, G.C., Nemoto, T., Miyashita, Y., Iino, M., and Kasai, H. (2001). Dendritic spine geometry is critical for AMPA receptor expression in hippocampal CA1 pyramidal neurons. Nat. Neurosci. *4*, 1086–1092.

Miller, J.P., Rall, W., and Rinzel, J. (1985). Synaptic amplification by active membrane in dendritic spines. Brain Res. *325*, 325–330.

Nicoll, R.A., and Roche, K.W. (2013). Long-term potentiation: peeling the onion. Neuropharmacology *74*, 18–22.

Padamsey, Z., McGuinness, L., Bardo, S.J., Reinhart, M., Tong, R., Hedegaard, A., Hart, M.L., and Emptage, N.J. (2017). Activity-Dependent Exocytosis of Lysosomes Regulates the Structural Plasticity of Dendritic Spines. Neuron *93*, 132–146.

Palmer, L.M., and Stuart, G.J. (2009). Membrane potential changes in dendritic spines during action potentials and synaptic input. J. Neurosci. *29*, 6897–6903.

Petersen, C.C.H. (2017). Whole-Cell Recording of Neuronal Membrane Potential during Behavior. Neuron *95*, 1266–1281.

Poleg-Polsky, A., and Diamond, J.S. (2011). Imperfect space clamp permits electrotonic interactions between inhibitory and excitatory synaptic conductances, distorting voltage clamp recordings. PLoS ONE *6*, e19463.

Popovic, M.A., Carnevale, N., Rozsa, B., and Zecevic, D. (2015). Electrical behaviour of dendritic spines as revealed by voltage imaging. Nat. Commun. *6*, 8436.

Rall, W. (1974). Dendritic spines, synaptic potency and neuronal plasticity. In Cellular Mechanisms Subserving Changes in Neuronal Activity, C.D. Woody, K.A. Brown, T.J. Crow, and J.D. Knispel, eds. (Brain Information Services), pp. 13–21.

Ramón y Cajal, S. (1888). Estructura de los centros nerviosos de las aves. Rev. Trim. Histol. Norm. Patol *1*, 1–10.

Sabatini, B.L., Oertner, T.G., and Svoboda, K. (2002). The life cycle of Ca(2+) ions in dendritic spines. Neuron *33*, 439–452.

Sato, T.K., Haider, B., Häusser, M., and Carandini, M. (2016). An excitatory basis for divisive normalization in visual cortex. Nat. Neurosci. *19*, 568–570.

Smith, M.A., Ellis-Davies, G.C., and Magee, J.C. (2003). Mechanism of the distance-dependent scaling of Schaffer collateral synapses in rat CA1 pyramidal neurons. J. Physiol. *548*, 245–258.

Spruston, N., Jaffe, D.B., Williams, S.H., and Johnston, D. (1993). Voltage- and space-clamp errors associated with the measurement of electrotonically remote synaptic events. J. Neurophysiol. *70*, 781–802.

Svoboda, K., Tank, D.W., and Denk, W. (1996). Direct measurement of coupling between dendritic spines and shafts. Science *272*, 716–719.

Tan, A.Y., and Wehr, M. (2009). Balanced tone-evoked synaptic excitation and inhibition in mouse auditory cortex. Neuroscience *163*, 1302–1315.

Tønnesen, J., Katona, G., Rózsa, B., and Nägerl, U.V. (2014). Spine neck plasticity regulates compartmentalization of synapses. Nat. Neurosci. *17*, 678–685.

Villa, K.L., Berry, K.P., Subramanian, J., Cha, J.W., Oh, W.C., Kwon, H.B., Kubota, Y., So, P.T., and Nedivi, E. (2016). Inhibitory Synapses Are Repeatedly Assembled and Removed at Persistent Sites In Vivo. Neuron *89*, 756–769.

Wehr, M., and Zador, A.M. (2003). Balanced inhibition underlies tuning and sharpens spike timing in auditory cortex. Nature *426*, 442–446.

Wilent, W.B., and Contreras, D. (2005). Dynamics of excitation and inhibition underlying stimulus selectivity in rat somatosensory cortex. Nat. Neurosci. *8*, 1364–1370.

Williams, S.R., and Mitchell, S.J. (2008). Direct measurement of somatic voltage clamp errors in central neurons. Nat. Neurosci. *11*, 790–798.

Wilson, C.J. (1984). Passive cable properties of dendritic spines and spiny neurons. J. Neurosci. *4*, 281–297.

Wu, G.K., Arbuckle, R., Liu, B.H., Tao, H.W., and Zhang, L.I. (2008). Lateral sharpening of cortical frequency tuning by approximately balanced inhibition. Neuron *58*, 132–143.

Yuste, R. (2013). Electrical compartmentalization in dendritic spines. Annu. Rev. Neurosci. *36*, 429–449.

Yuste, R., and Denk, W. (1995). Dendritic spines as basic functional units of neuronal integration. Nature *375*, 682–684.

STAR★METHODS

KEY RESOURCES TABLE

REAGENT or RESOURCE	SOURCE	IDENTIFIER
Experimental Models: Organisms/Strains		
Sprague Dawley rat	Charles River	Strain code: 400
Chemicals, Peptides and Recombinant Proteins		
Tetrodotoxin	Abcam	ab120055; CAS: 4368-28-9
Tetrodotoxin	Tocris	1078; CAS: 4368-28-9
D-APV	Tocris	0106; CAS: 79055-68-8
(+)-MK 801	Tocris	0924; CAS: 77086-22-7
DNQX disodium salt	Tocris	2312; CAS: 1312992-24-7
Picrotoxin	Tocris	1128; CAS: 124-87-8
Cyclopiazonic acid (CPA)	Sigma-Aldrich	C1530; CAS: 18172-33-3
Gly-Phe β-naphthylamide (GPN)	Abcam	Ab145914: CAS: 21438-66-4
MNI-caged-L-glutamate	Tocris	1490; CAS: 295325-62-1
Nimodipine	Sigma-Aldrich	N149; CAS:66085-59-4
Software and Algorithms		
MATLAB	MathWorks	RRID: SCR_001622
ImageJ	https://imagej.nih.gov/ij/index.html	RRID: SCR_003070

CONTACT FOR REAGENT AND RESOURCE SHARING

Further information and requests for resources and reagents should be directed to and will be fulfilled by the Lead Contact, Mark T. Harnett (harnett@mit.edu**)**.

EXPERIMENTAL MODEL AND SUBJECT DETAILS

Sprague Dawley rats (obtained from Charles River) were used for all experiments in accordance with NIH and the Massachusetts Institute of Technology Committee on Animal Care guidelines. Male rats were housed in pairs or singly and used for experimentation at 4.5-15 weeks of age.

METHOD DETAILS

Cortical Slice Preparation

Coronal brain slices (300 μm) from the somatosensory cortex were prepared from 4.5 to 15 week-old male Sprague-Dawley rats. Animals were deeply anesthetized with isoflurane prior to cardiac perfusion (using slicing solution described below) or immediate decapitation. Slicing was performed with a Vibratome (Leica) in ice-cold slicing solution containing (in mM): sucrose 90, NaCl 60, $NaHCO_3$ 26.5, KCl 2.75, NaH_2PO_4 1.25, $CaCl_2$ 1.1, $MgCl_2$ 5, glucose 9, sodium pyruvate 3, and ascorbic acid 1, saturated with 95% O_2 and 5% CO_2. Slices were incubated in artificial cerebrospinal fluid (aCSF) containing (in mM): NaCl 120, KCl 3, $NaHCO_3$ 25, NaH_2PO_4 1.25, $CaCl_2$ 1.2, $MgCl_2$ 1.2, glucose 11, sodium pyruvate 3, and ascorbic acid 1, saturated with 95% O_2 and 5% CO_2 at 35.5 °C for 25-30 min and then stored at 20 °C. All recordings were performed at 33–37 °C in aCSF.

Patch-Clamp Recording

An Olympus BX-61 epifluorescent microscope with infrared Dodt optics and a water-immersion lens (60×, 0.9 NA; Olympus) was used to visualize cells. Patch-clamp recordings were performed from apical trunk dendrites of layer 5 pyramidal neurons for most experiments. For experiments in Figures 3 and 4, recordings were restricted to large trunk dendrites close to the first branch point (659 ± 34 μm from soma, n = 11). Somatic recordings were used for experiments in Figure S4. Recordings were performed at resting membrane potential (zero injected current) for most experiments. Cells were held at −65 mV (< 1 nA holding current) for experiments in Figures 2D–2F and S4 when NMDA receptors were not blocked with D-APV and MK-801. Membrane potential was adjusted as indicated through steady-state current injections for experiments in Figures S3A–S3E.

Voltage-clamp whole-cell recordings were performed with an Axopatch 200B amplifier. Unless mentioned otherwise, series resistance and whole-cell capacitance were predicted and compensated >90% with lag < 10 μs. The prediction and compensation were set as high as possible with the lag as short as possible (up until the recording began oscillating) such that less than 1 MΩ was left uncompensated. We were able to fully compensate, and even overcompensate in some cases the series resistance (recovering more current than injected and causing negative voltage deflections). Current-clamp recordings were performed in bridge mode with an Axopatch 200B or a Dagan BVC-700 amplifier with bridge fully balanced. Current and voltage signals were filtered at 10 kHz and digitized at 20 kHz. Patch pipettes made out of thick-wall glass (1.5 O.D., 0.75 I.D.) were used for voltage-clamp recordings to reduce capacitance. Current-clamp patch pipettes were prepared with thick-wall or thin-wall glass (1.5 O.D., 1.1 I.D.). Pipettes had resistances ranging from 2 to 8 MΩ and the capacitance was fully neutralized prior to break in. Particular care was taken to keep series resistances very low; it ranged from 3 to 20 MΩ and the recording was aborted if it rose above 20 MΩ. In dual dendritic recordings, the voltage waveform on the voltage measuring electrode was used as an independent reference to adjust the series resistance on the current-passing electrode with both electrodes in current clamp. Final adjustments for the series resistance were made offline to correct for small residual errors (< 1.25 MΩ) for experiments in Figures 2A–2C and S2A–S2G.

The standard intracellular solution contained (in mM): potassium gluconate 134, KCl 6, HEPES buffer 10, NaCl 4, Mg_2ATP 4, NaGTP 3, phosphocreatine di (tris) 14. For experiments in Figures 3, 4, S1I–S1K, S2H–S2N and S3F–S3I, a cesium-based intracellular solution was used (in mM): Cs-methanesulfonate 140, KCl 3, HEPES buffer 10, NaCl 4, Mg_2ATP 4, NaGTP 3, phosphocreatine di (tris) 14. Depending on the experiment, 0.05 Alexa 594, 0.1 Alexa 488 and/or 0.2 Fluo-4 mM (Invitrogen) were added to the intracellular solution. Liquid junction potentials (16.2 and 12.3 mV for standard and cesium intracellular, respectively) were not corrected for.

Two-Photon Imaging and Uncaging

A two-photon laser scanning system (Prairie Technologies) with dual galvanometers and two Mai Tai DeepSee lasers were used to simultaneously image and uncage glutamate. One path was used to image Alexa 594 at 880 nm or Fluo-4 and Alexa 488 at 920 nm (separated via dichroic mirrors to independent GaAsP PMTs). Linescan imaging of spines and dendrites was performed at 700-1300 Hz with dwell times of 8 μs for < 400 ms. The other path was used to photolyse 4-methoxy-7-nitroindolinyl-caged-L-glutamate (MNI-glutamate) at 720 nM. Stock MNI solutions (50 mM) were freshly diluted in aCSF to 10 mM and applied via pressure ejection through a large glass pipette above the slice. Laser beam intensity was independently controlled with electro-optical modulators (model 350-50; Conoptics). Uncaging dwell time was 0.2 ms. For experiments involving near-simultaneous activation of multiple spines (Figure S4), the interval between spines was 0.32 ms (0.2 ms dwell time and 0.12 ms moving time). A passive 8X pulse splitter in the uncaging path was used to reduce photodamage (Harnett et al., 2013; Ji et al., 2008). Experiments were terminated if signs of photodamage were detected (increase in basal fluorescence, loss of transient signals and/or depolarization). Given the resolution of two-photon microscopy and the high brightness of large layer 5 apical dendrites, spine morphology could not be quantitatively assessed. Thus, no attempt was made at correlating physiological results with morphological parameters. Selected spines were within 10 μm from the voltage-clamp electrode unless mentioned otherwise. Care was taken to ensure that the selected spines were well isolated (no spines within 1 μm laterally and no spines above or below in z; Figure S2).

Pharmacology

TTX, D-APV, MK-801 and DNQX dissolved in water, nimodipine dissolved in methanol as well as cyclopiazonic acid (CPA) and Gly-Phe β-naphthylamide (GPN) dissolved in DMSO were prepared as stock solutions stored at −20 °C and diluted directly to the aCSF on the day of the experiment. $NiCl_2$ and $CdCl_2$ were weighed and freshly dissolved in aCSF. Picrotoxin was weighed, dissolved in aCSF and sonicated on the day of the experiment. For all experiments, 0.5 μM TTX was added to the recording aCSF to block voltage-gated sodium channels. For constant blockade of NMDA receptors (Figures 3, 4, S2H-S2N, S3F-S3I and where noted in S4), 50–100 μM D-APV and 10-25 μM MK-801 were present in both the aCSF and the glutamate puffer pipette. For acute blockade of NMDA receptors (Figures 2G and 2H), 100 μM D-APV and 50 μM MK-801 were washed on for over 10 min through the bath. DNQX (20 μM), nimodipine (20 μM) and $NiCl_2$ (300 μM) were present for experiments in Figures S3A–S3E. For Figures S3F and S3G, nimodipine (20 μM) and $NiCl_2$ (300 μM) were washed on through the bath for >10 min and the glutamate puffer pipette was exchanged to include the drugs. CPA (30 μM) and GPN (200 μM) were washed on for over 30 min through the bath in Figures S3H and S3I. Reversal potential (E_{syn}) was measured with $CdCl_2$ (200 μM) in the bath solution to prevent Ca^{2+} spikes and stabilize the membrane potential. For recording mEPSPs, a patch pipette filled with aCSF plus 300 mOsm of sucrose (~600 mOsm final) and Alexa 488 was brought close to the dendrite (~5 μm from the recording electrode). Low-pressure ejection was used to create a ~10 μm cloud around the recording pipette to locally induce presynaptic release. Picrotoxin (100 μM) was added to the bath solution for recording mEPSPs.

Compartmental Modeling

Simulations were performed in MATLAB. The model consisted of a cylindrical soma (diameter = 25 μm, length = 25 μm) and a 1.2 mm apical dendrite (tapered diameter from 7 to 4 μm). The parameters were set to reflect the apical trunk of L5 dendrites under the experimental conditions of Figures 3 and 4 where NMDA, voltage-gated sodium channels and voltage-gated potassium channels were blocked (Figures S1I–S1K). A spine with a head diameter of 0.5 μm was attached on the dendrite 600 μm from the soma. The model included a membrane capacitance of 1.2 μF cm^{-2} and an axial resistivity of 100 Ω*cm. The membrane resistivity was 20,000 Ω*cm^2

at the soma and dropped linearly as a function of distance to 3000 Ω*cm^2 at a distance of 566 μm and beyond. Spine capacitance as well as spine head resistance had negligible impacts on the dynamics studied (< 0.2% change with 5-fold manipulations).

Resting membrane potential was −80 mV. AMPA synapses were simulated as rapid conductance changes in the spine head, while a dendritic electrode was in current clamp, where the membrane voltage could fluctuate freely, or ideal voltage clamp, where the voltage is kept constant. Voltage clamp was implemented in the dendritic compartment adjacent to the spine. AMPA conductance was modeled as a double-exponential function (Harnett et al., 2012) with 0.1 ms rise time constant, 0.75 ms decay time constant and reversal potential at 0 mV to produce EPSPs with kinetics matching the experimental mEPSPs (Figure S1K). Inhibitory synapses (Figure S5) were simulated like AMPA synapses but the reversal potential was set to −80mV.

Determination of R_{neck} and g_{syn}

The synaptic conductance is a function of the time-varying synaptic current and the driving force:

$$g_{syn} = \frac{I_{syn}}{E_{syn} - V_{spine}} \quad (1)$$

Considering the spine and the dendrite as two compartments linked by R_{neck}, the current flowing across the neck is a function of the voltage difference between the two compartments and the resistance linking them:

$$I_{dend} = \frac{V_{spine} - V_{dend}}{R_{neck}} \quad (2)$$

Under dendritic voltage clamp, the current entering the dendrite is faithfully recovered (I_{rec}) and the dendritic voltage is kept constant ($\Delta V_{dend} = 0$; Figure S1 and S2). The difference between V_{spine} and V_{dend} thus corresponds to the unclamped spine EPSP. Equation 2 can therefore be simplified to Equation 3, which is illustrated in Figures 3A and 3B:

$$I_{rec} = \frac{\text{Spine EPSP}}{R_{neck}} \quad (3)$$

The current entering the spine flows into the dendrite without loss or time delay (Figure S1; (Koch and Poggio, 1983; Wilson, 1984)). Thus $I_{syn} = I_{rec}$. From Equations 1 and 3, we get Equation 4, which is illustrated in Figure 4B:

$$g_{syn} = \frac{I_{rec}}{E_{syn} - V_{spine}} \quad (4)$$

For estimating the spine EPSP with dendritic current injections, several criteria were used to ensure a good fit in terms of the aEPSP kinetics and Ca^{2+} signal amplitude. For the aEPSP matching the kinetics of the uEPSC, the correlation coefficient threshold was >0.95. For Ca^{2+} signals, the difference was < 0.05 ΔF/F. 10 out of 16 spines analyzed met those criteria. When E_{syn} - V_{spine} approaches 0, g_{syn} estimates are more prone to errors. To avoid such errors, we only computed g_{syn} when saturation was below 80% (7 out of 10 spines). For 3 spines with saturation above 80%, we made a conservative estimate that synaptic conductance was >8 nS based on the relationship between g_{syn} and saturation in our model (see Figures 1 and S1).

QUANTIFICATION AND STATISTICAL ANALYSES

Analysis was performed using custom-written MATLAB codes. Current and voltage signals were filtered at 2 kHz with zero-phase filtering using the MATLAB function filtfilt for some experiments. Linescan signals were smoothed using a 3-point moving average. Some imaging trials exhibited a light artifact from the uncaging laser, which was excised. 2-5 trials were acquired per condition and averaged for both electrophysiological and optical traces (see Figure S2N). Morphological and distance measurements were performed using ImageJ/FIJI (National Institutes of Health) on two-dimensional maximal intensity projections of 1–2 μm Z series collected at the end of the experiment. Miniature EPSPs were detected by fitting template EPSPs to events with fast 20%–80% rise times (median: 0.55 ms, Q1-Q3: 0.45-0.65 ms, n = 2285; excluded if >1.5 ms).

Statistical analysis was performed in MATLAB. D'Agostino-Pearson test was used to assess normality. For normal data, results are presented as mean ± SEM and two-tailed t test was used for statistical analyses. For skewed data, the median and the lower and upper quartiles (Q1-Q3) are reported and Wilcoxon paired test was used for statistical comparisons. Statistical details can be found in the figure legends and in the Results. Reported n values refer to the number of spines unless indicated otherwise.